Geoelectromagnetic induction in a heterogeneous sphere: a new three-dimensional forward solver using a conservative staggered-grid finite difference method

M. Uyeshima[1] and A. Schultz[2]

[1] *Earthquake Research Institute, University of Tokyo, 1-1-1 Yayoi, Bunkyo, Tokyo, 113–0032, Japan. E-mail: uyeshima@utada-sun.eri.u-tokyo.ac.jp*
[2] *Institute of Theoretical Geophysics, Department of Earth Sciences, University of Cambridge, Cambridge, CB2 3EQ, UK. E-mail: adam@itg.cam.ac.uk*

SUMMARY

A conservative staggered-grid finite difference method is presented for computing the electromagnetic induction response of an arbitrary heterogeneous conducting sphere by external current excitation. This method is appropriate as the forward solution for the problem of determining the electrical conductivity of the Earth's deep interior. This solution in spherical geometry is derived from that originally presented by Mackie *et al.* (1994) for Cartesian geometry. The difference equations that we solve are second order in the magnetic field **H**, and are derived from the integral form of Maxwell's equations on a staggered grid in spherical coordinates. The resulting matrix system of equations is sparse, symmetric, real everywhere except along the diagonal and ill-conditioned. The system is solved using the minimum residual conjugate gradient method with preconditioning by incomplete Cholesky decomposition of the diagonal sub-blocks of the coefficient matrix. In order to ensure there is zero **H** divergence in the solution, corrections are made to the **H** field every few iterations. In order to validate the code, we compare our results against an integral equation solution for an azimuthally symmetric, buried thin spherical shell model (Kuvshinov & Pankratov 1994), and against a quasi-analytic solution for an azimuthally asymmetric configuration of eccentrically nested spheres (Martinec 1998).

Key words: electrical conductivity, electromagnetic induction, electromagnetic modelling, mantle, numerical techniques.

1 INTRODUCTION

Seismology and electromagnetic induction provide the only means of propagating energy into the Earth's deep interior, and using this to sense the internal structure and properties of the mantle from observations at the surface. Realistic estimates of the radial dependence of the electrical conductivity of the upper mantle have been available for 60 years (Lahiri & Price 1939; Banks 1969). Historically, no methods were available to model the lateral heterogeneity of global-scale mantle conductivity structure, nor were digital catalogues of geomagnetic observatory data of sufficient spatial density and quality to warrant such analysis. This has greatly diminished the role played by electromagnetic methods in geodynamical studies of the Earth's deep interior. Rather, our present knowledge of the upper and mid-mantle comes primarily from seismology, and our understanding of this region is based largely on its elastic parameters.

The electrical conductivity of the materials comprising the Earth's mantle is strongly dependent upon temperature, but it is also an indicator of state (e.g. partial fraction of melt), composition (e.g. iron content) and the presence of volatiles. The electrical conductivity in the mid-mantle increases with depth, particularly near the 410 km seismic discontinuity, and near and below the 660 km discontinuity (Schultz *et al.* 1993; Xu *et al.* 1998a,b; Olsen 1999).

Strong lateral heterogeneity has been detected in mantle electrical conductivity. Geographically distributed response functions have been calculated in the period range 2 days to 1 year, under the assumption that the source fields arise from the relaxation phase of D_{st} activity. Such response functions have been found to be simultaneously consistent with regional 1-D earth structure, and at mid-latitudes with $\cos \theta$ colatitudinal dependence of the source potential (Schultz & Larsen 1987). It has been established formally that no global 1-D model exists that fits this global magnetic observatory data set to within statistical bounds (Schultz & Larsen 1990). Furthermore, analysis of 1-D conductivity sounding profiles calculated from magnetic observatory data reveals significant regional variability (Schultz 1990).

Recently, deep magnetotelluric (MT) experiments have been conducted that have substantially increased the resolving power of EM investigations of the upper mantle. These have included multiyear experiments on continents using long electric dipoles (Egbert *et al.* 1992; Egbert & Booker 1992; Schultz *et al.* 1993; Bahr *et al.* 1993), and also seafloor experiments employing abandoned submarine telecommunications cables (Lizarralde *et al.* 1995; Fujii *et al.* 1995). A correspondence between patterns of electrical heterogeneity and tectonic regime (e.g. Lizarralde *et al.* 1995; Schultz & Semenov 1993) has been observed. Such experiments confirm that there are substantial levels of lateral electrical heterogeneity in the upper mantle. Petrological evidence as well as laboratory results applied to samples of olivine of varying composition (e.g. Hirsch *et al.* 1993; Hirsch & Shankland 1993) also sustain this view. Lateral variations in conductivity are expected as regionally distinct geotherms are mapped into regional variabilities in electrical conductivity.

This recent progress in regional deep conductivity investigations has stimulated renewed interest in conduction mechanisms in the upper mantle through the transition zone. Enhanced electrical conduction can result from the presence of hydrogen, and the contamination by volatiles of the impure semiconductors comprising the upper mantle (Bai & Kohlstedt 1993; Karato 1990; Shankland & Duba 1997). A 'wet' rather than 'dry' olivine model has therefore been proposed to account for elevated upper mantle conductance (Schultz *et al.* 1993; Lizarralde *et al.* 1995), particularly at depths between 200 and 410 km.

The upper mantle mineral $Mg_{1.8}Fe_{0.2}SiO_4$ olivine transforms to the polymorph wadsleyite at pressures corresponding to 410 km depth, and to ringwoodite at approximately 520 km depth, finally disproportionating to (Mg,Fe)-SiO_3 perovskite + $(Mg,Fe)O$ at depths near 660 km. Both upper mantle polymorphs have been found to have nearly two orders of magnitude higher conductivity than olivine (Xu *et al.* 1998). This may also help to reconcile the difference between laboratory measurements for dry single-crystal olivine and field observations that require a higher upper mantle conductance. Xu *et al.* (1998) suggested that a conductivity jump of roughly two orders of magnitude between 400 and 500 km, observed by Schultz *et al.* (1993) beneath the central Canadian Shield, may primarily reflect the phase transition between olivine and wadsleyite at 410 km.

The upper mantle conductivity is therefore expected to contain the signature of thermally activated electrical conduction processes, of mineral phase transitions, as well as of the time-integrated effects of mantle convection. This is expressed through contamination of the upper mantle by lithospheric materials introduced through plate subduction. Above the transition zone, the effect of thermal gradients and the presence of volatiles and melt may lead to variations in conductivity of several orders of magnitude across a given convection cell. In contrast, lateral variations in electrical conductivity in the lower mantle may be less than one order of magnitude (Shankland *et al.* 1993).

The mineralogical and experimental case for substantial heterogeneity in upper mantle conductivity has stimulated the development of methods for solving Maxwell's equations in a heterogeneous conducting sphere. Such forward solutions, if suitably accurate, may then be used as the basis for inverse solvers used to reconstruct the electrical conductivity distribution in the upper to mid-mantle. At the present time, regional scalar electromagnetic response functions are available (e.g. Schultz & Larsen 1987) that have been calculated with statistical uncertainties (standard errors) of 3–5 per cent. More recent analysis of a greatly expanded geomagnetic database, taking into account a more sophisticated source field model (Fujii & Schultz 1998) is considerably enlarging the geographical coverage of such response functions. This work will ultimately result in increased sensitivity to 3-D structure in the mantle.

The statistical confidence level for these new more geographically complete response estimates is similar to those calculated previously. Given that the response functions are calculated from ratios of field components, or ratios of spatial gradients in the fields (Olsen 1998; Schultz & Zhang 1994), it is necessary to calculate the fields from a given model with an accuracy substantially better than the level of uncertainty in the observed response functions. For the present work, we deem a forward solution to be suitably accurate if, upon comparison with the other numerical or (quasi-)analytical solutions, the mismatch between the anomalous part of the calculated fields at the Earth's surface is within 1 per cent.

The realization that electromagnetic induction methods may play a renewed role in deep geodynamical investigations has led several workers recently to develop new 3-D forward solution methods. Zhang & Schultz (1992) introduced a vector Helmholtz equation formulation based on the solution of the perturbation of the potentials about an underlying 1-D solution. Schultz & Pritchard (1998) used this approach as the basis for generating the first 3-D inverse model of the conductivity of the upper and mid-mantle. A larger degree of heterogeneity was found to be required for some regions than could be accommodated accurately by the perturbation method, leading to an acceptable rms misfit of approximately 1.0 at most locations, but a statistically undesirable global rms misfit of approximately 2.0.

Everett & Schultz (1996) devised a 3-D finite element forward solution using spherical polyhedra. This approach was free from the perturbation expansion restriction of mild lateral conductivity heterogeneities. Tarits *et al.* (1999) have devised a spectral solution for a 3-D heterogeneous earth suitable for examining internal induction due to time-varying currents in the core, and also external induction due to magnetospheric and ionospheric current sources. Martinec (1999) has recently applied a spectral–finite element approach to the problem of external electromagnetic induction in an arbitrary heterogeneous conducting sphere. A variety of special solutions have also been devised, including quasi-analytical solutions for axisymmetric eccentrically nested conducting spheres (Everett & Schultz 1995); asymmetric eccentrically nested spheres (Martinec 1998); a buried shell (Kuvshinov & Pankratov 1994) and multishells (Kuvshinov *et al.* 1998), which are based on the modified iterative–dissipative method (Singer 1995). Recently, Koyama & Utada (1998) have applied this method to the problem of an arbitrary heterogeneous conducting sphere. The existence of such a range of forward solutions makes it feasible to compare the various new forward solvers against each other, and against potentially accurate quasi-analytic solutions. Such a project involving all the principal groups working in this area (those referenced above, as well as other workers in Russia and the USA) is currently underway, and the results will be reported in a subsequent publication.

The recognition that some of the newly developed 3-D forward solutions may not be sufficiently accurate to calculate fields to 1 per cent of their theoretical value has lead us to consider an alternative method. Mackie *et al.* (1993) and Mackie *et al.* (1994) have developed an accurate and numerically efficient solution for the electromagnetic fields due to an arbitrary heterogeneous earth in Cartesian coordinates. We have used the framework of this method as the basis for a new solution for the fields due to an electrically heterogeneous earth in spherical coordinates. We have devised a means by which the symmetry properties of the original Cartesian solution may be maintained, and have applied a new set of boundary conditions peculiar to a spherical earth. We shall demonstrate in the present paper that we have achieved the requisite accuracy in the magnetic fields at the earth's surface by using this latest method. In so doing, we show that an efficient and accurate 3-D forward solution exists that may be applied to the inverse problem of reconstructing the heterogeneities in electrical conductivity in the upper and mid-mantle.

2   DIFFERENCE EQUATIONS FOR STAGGERED GRIDS IN SPHERICAL COORDINATES

For deep global geoelectromagnetic induction investigations, we have made use of response functions in the period range $2 \, \text{day} \leq T \leq 1 \, \text{yr}$. This period range corresponds to penetration depths spanning approximately 300–1500 km. At these long periods, given that the electrical conductivity of the air layer is higher than $10^{-14} \, \text{S m}^{-1}$ (e.g. Rokityansky 1982), and given that the dielectric constant is $\sim 10^{-11} \, \text{F m}^{-1}$ everywhere, conduction currents dominate over displacement currents throughout the air–earth domain. Thus, the integral form of Maxwell's equations (assuming $e^{i\omega t}$ harmonic time dependence) is given by

$$\oint \mathbf{H} \cdot d\mathbf{l} = \iint \mathbf{J} \cdot d\mathbf{S}, \tag{1}$$

$$\oint \mathbf{E} \cdot d\mathbf{l} = -\iint i\omega\mu\mathbf{H} \cdot d\mathbf{S}, \tag{2}$$

$$\mathbf{J} = \sigma\mathbf{E}, \tag{3}$$

where $\mathbf{H}$, $\mathbf{E}$ and $\mathbf{J}$ denote the magnetic and electric fields and the electric current density, and ω, σ and μ are the angular frequency, electrical conductivity and magnetic permeability, respectively. We assume that the electrical conductivity is isotropic, but the generalization to anisotropic media is straightforward. The magnetic permeability is assumed to be that of a vacuum ($4\pi \times 10^{-7} \, \text{H m}^{-1}$) everywhere. $d\mathbf{l}$ is a line element and $d\mathbf{S}$ ($= \mathbf{n}dS$) is a surface element that is defined on a surface enclosed by the contour of $d\mathbf{l}$ and orthogonal to the element of the surface. The sign convention for the direction of $\mathbf{n}$ is taken so that $\mathbf{n}$ and $d\mathbf{l}$ satisfy the right-hand rule.

Although the electrical conductivity of the air layer is often assumed to be zero, we find it convenient to follow Mackie *et al.* (1993) and assign to it a moderately small non-zero value ($10^{-10} \, \text{S m}^{-1}$). By so doing, the Helmholtz equation holds throughout the model domain and the matrix system used in the forward solution remains acceptably well conditioned, as will be discussed later. Were the usual assumption taken that $\sigma_{\text{air}} = 0$ (e.g. Everett & Schultz 1996), then at low frequencies Laplace's equation would hold in the air layer, and the Helmholtz equation would hold in the conducting earth below. This presents the added complication of needing to match boundary conditions at the air–earth interface.

On the top of the air layer (the outermost portion of the computational domain), an appropriate source field configuration is set by assigning values to the contour integrals of the tangential components of the $\mathbf{H}$ field. That is, we solve a Dirichlet boundary value problem. In all the test cases shown later, the external source structure we use is the P_1^0 configuration, that is, the structure that predominates for external current systems related to the equatorial magnetospheric ring current (Schultz 1990). The air layer should be extended far enough above the earth for all of the secondary, internally induced $\mathbf{H}$ field perturbations to be damped out at the location of the source. In the present paper, we locate the source $\mathbf{H}$ field at a distance of $10r_e$ from the earth's centre. The appropriateness of this configuration is discussed further in Appendix A.

The core–mantle boundary (CMB) is taken to be the bottom of the computational domain. In the core, the conductivity is set to be infinite, which has the effect of forcing $\mathbf{H}$ within the core's interior to vanish identically. We therefore set, as boundary conditions, $\mathbf{H} = 0$ at the bottom of our computation domain in the core, whilst immediately on the CMB tangential $\mathbf{H}$ field components $\neq 0$ (the values of which are calculated). In reality, the strong attenuation of externally induced fields in the conducting mantle leads all components of $\mathbf{H}$ in the vicinity of the CMB to be approximately zero.

In order to obtain solutions of $\mathbf{H}$ directly for the geoelectromagnetic induction problem in spherical coordinates, a second-order difference equation in terms of $\mathbf{H}$ is derived based on the staggered grid method. This has been applied previously only to the Cartesian problem (Visscher 1989; Mackie *et al.* 1993). In Fig. 1, the mesh division geometry is shown for the staggered-grid finite difference method in spherical coordinates. The whole computational domain including the resistive air and conductive earth is divided into curved rectangular prisms. Each prism is bounded by latitudinal, longitudinal and radial edges along which $\mathbf{H}$ field components in the respective edge directions are defined. We name these prisms, edges and nodes *H-prisms*, *H-edges* and *H-nodes*, respectively. Conductivity values are defined to be uniform in the respective *H-prisms*. We also define staggered prisms (or *E-prisms*) whose nodes (*E-nodes*) are located at the centre of the respective *H-prisms* and whose edges (*E-edges*) cut halfway through *H-surfaces*. We name the surfaces of the *H-* and *E-prisms H-* and *E-surfaces*. Due to the orthogonality of the spherical coordinate system, sets of *H-surfaces* and *E-edges* so defined, together with the sets of *E-surfaces* and *H-edges* are always mutually perpendicular. Latitudinal, longitudinal and radial components of $\mathbf{J}$ and $\mathbf{E}$ are defined along the *E-edges* and are thus tangential to surfaces of *H-prisms*.

Hereafter, $\phi(i)$, $\theta(j)$ and $r(k)$ specify longitude, colatitude and distance from the earth's centre for the *ijk*th *H-node* position. The index i ranges from $[1, L]$ and is numbered from west to east, with the zero meridian $\phi = 0$ associated with $i = 1$ and $i = L + 1$. Index j ranges from $[1, M + 1]$ with $j = 1$ representing an *H-node* position at the north pole ($\theta = 0$), and $j = M + 1$ the south pole ($\theta = \pi$). Index k ranges from $[1, N + 1]$ with $k = 1$ at the top of the air layer ($r = 10r_e$), and
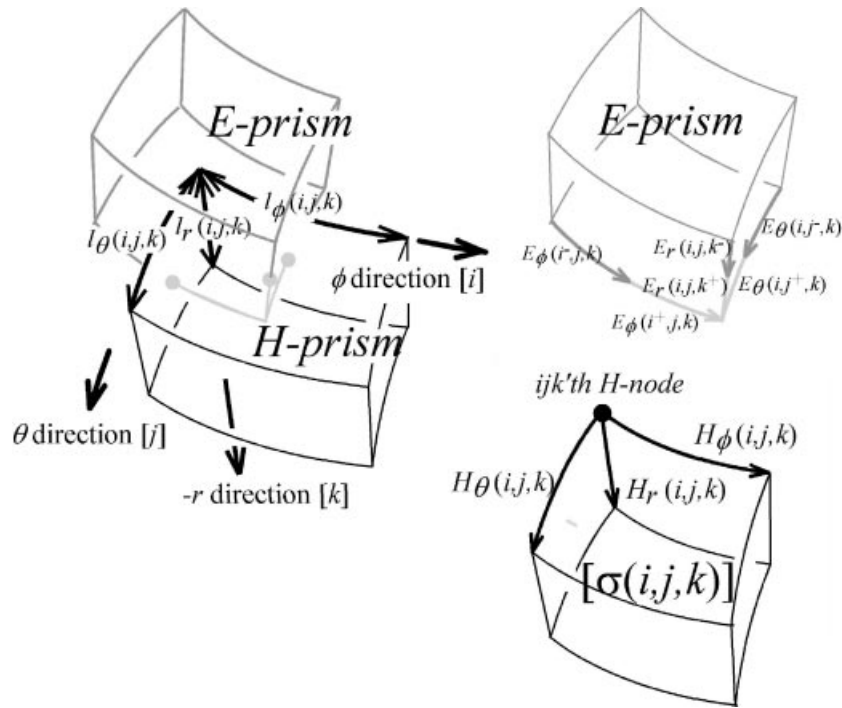
Figure 1. The mesh division geometry for the staggered-grid finite difference formulation designed for the geoelectromagnetic induction problem in spherical coordinates. The whole computational domain including the resistive air and conductive earth is divided into curved rectangular prisms. This primary prism (*H-prism* drawn with solid curves on the left-hand side and at the bottom on the right-hand side) is bounded by latitudinal, longitudinal and radial edges along which **H** field components are defined. Conductivity values are defined to be uniform in the respective *H-prisms*. Staggered prisms (*E-prisms* drawn with shaded curves on the left-hand side and at the top on the right-hand side) are also defined whose nodes are located at the centre of the respective *H-prisms* and whose edges cut halfway through *H-surfaces*. In coordinate indices for the **E** field components, (−) means outside the *H-prism* of uniform conductivity $\sigma(i, j, k)$ and (+) means inside that prism. See text for a more detailed explanation.

$k = N + 1$ just within the earth's perfectly conducting core ($r = 3480$ km). The numbers of *H-prisms* are assumed to be L, M and N in the ϕ-, θ- and r-directions, respectively.

$H_\phi(i, j, k)$, $H_\theta(i, j, k)$ and $H_r(i, j, k)$ denote the respective components of the magnetic field defined along the *ijk*th *H-edge*. In order to relate the fields to right-handed coordinates, r-components of **H**, **E** and **J** are taken to be positive when pointing towards the centre of the earth. Lengths of the *ijk*th *H-edges* in the respective directions are defined as $l_\phi(i, j, k)$, $l_\theta(i, j, k)$ and $l_r(i, j, k)$ and are given by

$$l_\phi(i, j, k) = r(k) \sin \theta(j) [\phi(i + 1) - \phi(i)],$$

$$l_\theta(i, j, k) = r(k) [\theta(j + 1) - \theta(j)], \tag{4}$$

$$l_r(i, j, k) = r(k) - r(k + 1).$$

Given that the **H** field components are defined on the *H-edges* rather than the *H-nodes*, the coordinate indices for H and l should differ from those defined above. That is, for $H_\phi(i, j, k)$ and $l_\phi(i, j, k)$, index i ranges from $[1, L]$, j from $[2, M]$ and k from $[1, N + 1]$. H_ϕ is not defined on the staggered grid at the poles (i.e. $j = 1$ or $M + 1$). For $H_\theta(i, j, k)$ and $l_\theta(i, j, k)$, i ranges from $[1, L]$, j from $[1, M]$ and k from $[1, N + 1]$. The indexing for $H_r(i, j, k)$ and $l_r(i, j, k)$ must take into account the poles (i.e. $i = 1$, and $j = 1$ or $M + 1$), where k ranges from $[1, N]$. For non-polar positions, i ranges from $[1, L]$, j from $[2, M]$ and k from $[1, N]$.

The **J** components are represented as $J_\phi(i, j, k)$, $J_\theta(i, j, k)$ and $J_r(i, j, k)$, where, e.g. $J_\theta(i, j, k)$ is defined on the *H-surface*

enclosed with the *ijk*th and $[i + 1]jk$th *H-edges* in the r-direction and the *ijk*th and $ij[k + 1]$th *H-edges* in the ϕ-direction, or it is defined along an *E-edge* crossing above the *H-surface* at its centre. The length of this *E-edge* can be calculated by

$$\frac{1}{2} l_\theta(i^+, j - 1, k^+) + \frac{1}{2} l_\theta(i^+, j, k^+)$$

$$= \frac{1}{2} r(k^+) [\theta(j) - \theta(j - 1)] + \frac{1}{2} r(k^+) [\theta(j + 1) - \theta(j)]. \tag{5}$$

Here i^+ represents the $(i + 1/2)$th *E-node* or edge, and the coordinate $[\phi(i^+), \theta(j), r(k^+)]$ represents the centre of the *H-surface* where $J_\theta(i, j, k)$ is defined. Similarly, we will also use i^- to represent the $(i − 1/2)$th *E-node* (see Fig. 1). The area of this *H-surface* normal to the θ-direction is denoted as $S_\theta(i, j, k)$ and is calculated by

$$S_\theta(i, j, k) = \frac{1}{2} [r(k)^2 - r(k + 1)^2] \sin \theta(j) [\phi(i + 1) - \phi(i)]. \tag{6}$$

Areas of the *H-surfaces* normal to the other directions are also calculated by

$$S_\phi(i, j, k) = \frac{1}{2} [r(k)^2 - r(k + 1)^2] [\theta(j + 1) - \theta(j)],$$

$$S_r(i, j, k) = r(k)^2 [\cos \theta(j) - \cos \theta(j + 1)] [\phi(i + 1) - \phi(i)]. \tag{7}$$

Similarly, the area of the respective *E-surface* enclosing the *E-prism* is defined as $S_\phi(i_+, j^-, k^-)$. Since the **E** field component

normal to the boundary of cells of different conductivity is discontinuous across the boundary (due to Ohm's Law, e.g. eq. 3), **E** should be defined separately for the plus- and minus-sides of the boundary, whereas the **J** component is continuous. Thus, the **E** field components corresponding to $J_\theta(i, j, k)$ are $E_\theta(i, j^-, k)$ and $E_\theta(i, j^+, k)$.

With this mesh division scheme and notation, the integral form of Ampere's Law (eq. 1) for a small loop in the tangential plane can be represented as

$$l_\phi(i, j, k)H_\phi(i, j, k) + l_\theta(i+1, j, k)H_\theta(i+1, j, k)$$
$$- l_\phi(i, j+1, k)H_\phi(i, j+1, k) - l_\theta(i, j, k)H_\theta(i, j, k)$$
$$= J_r(i, j, k)S_r(i, j, k). \tag{8}$$

Similar equations to (8) for the other small loops in the meridional and latitudinal planes can be written, respectively, as

$$l_\theta(i, j, k)H_\theta(i, j, k) + l_r(i, j+1, k)H_r(i, j+1, k)$$
$$- l_\theta(i, j, k+1)H_\theta(i, j, k+1) - l_r(i, j, k)H_r(i, j, k)$$
$$= J_\phi(i, j, k)S_\phi(i, j, k) \tag{9}$$

and

$$l_r(i, j, k)H_r(i, j, k) + l_\phi(i, j, k+1)H_\phi(i, j, k+1)$$
$$- l_r(i+1, j, k)H_r(i+1, j, k) - l_\phi(i, j, k)H_\phi(i, j, k)$$
$$= J_\theta(i, j, k)S_\theta(i, j, k). \tag{10}$$

The discrete form of Faraday's Law (eq. 2) for a small loop in the meridional plane is written

$$-\frac{l_r(i^+, j^-, k)}{2}E_r(i, j-1, k^+) - \frac{l_r(i^+, j^-, k-1)}{2}E_r(i, j-1, k^-)$$
$$+ \frac{l_\theta(i^+, j-1, k^-)}{2}E_\theta(i, j^-, k-1)$$
$$+ \frac{l_\theta(i^+, j, k^-)}{2}E_\theta(i, j^+, k-1)$$
$$+ \frac{l_r(i^+, j^+, k-1)}{2}E_r(i, j, k^-) + \frac{l_r(i^+, j^+, k)}{2}E_r(i, j, k^+)$$
$$- \frac{l_\theta(i^+, j, k^+)}{2}E_\theta(i, j^+, k) - \frac{l_\theta(i^+, j-1, k^+)}{2}E_\theta(i, j^-, k)$$
$$= -i\omega\mu S_\phi(i^+, j^-, k^-)H_\phi(i, j, k). \tag{11}$$

Equations similar to (11) for the other small loops in the latitudinal and the tangential planes are given as

$$-\frac{l_\phi(i, j^+, k^-)}{2}E_\phi(i^+, j, k-1) - \frac{l_\phi(i-1, j^+, k^-)}{2}E_\phi(i^-, j, k-1)$$
$$+ \frac{l_r(i^-, j^+, k-1)}{2}E_r(i-1, j, k^-)$$
$$+ \frac{l_r(i^-, j^+, k)}{2}E_r(i-1, j, k^+)$$
$$+ \frac{l_\phi(i-1, j^+, k^+)}{2}E_\phi(i^-, j, k) + \frac{l_\phi(i, j^+, k^+)}{2}E_\phi(i^+, j, k)$$
$$- \frac{l_r(i^+, j^+, k)}{2}E_r(i, j, k^+) - \frac{l_r(i^+, j^+, k-1)}{2}E_r(i, j, k^-)$$
$$= -i\omega\mu S_\theta(i^-, j^+, k^-)H_\theta(i, j, k) \tag{12}$$

and

$$-\frac{l_\theta(i^-, j, k^+)}{2}E_\theta(i-1, j^+, k) - \frac{l_\theta(i^-, j-1, k^+)}{2}E_\theta(i-1, j^-, k)$$
$$+ \frac{l_\phi(i-1, j^-, k^+)}{2}E_\phi(i^-, j-1, k)$$
$$+ \frac{l_\phi(i, j^-, k^+)}{2}E_\phi(i^+, j-1, k)$$
$$+ \frac{l_\theta(i^+, j-1, k^+)}{2}E_\theta(i, j^-, k) + \frac{l_\theta(i^+, j, k^+)}{2}E_\theta(i, j^+, k)$$
$$- \frac{l_\phi(i, j^+, k^+)}{2}E_\phi(i^+, j, k) - \frac{l_\phi(i-1, j^+, k^+)}{2}E_\phi(i^-, j, k)$$
$$= -i\omega\mu S_r(i^-, j^-, k^+)H_r(i, j, k). \tag{13}$$

In (11)–(13), the upper halves of the vertical segments are associated with $E_r(, , k^-)$ above the respective tangential *H-surface*, and the lower halves with $E_r(, , k^+)$ below that surface. This allows for a discontinuous change of E_r across the *H-prism* boundaries. Similarly, $E_\phi(i^-, ,)$ and $E_\phi(i^+, ,)$ are, respectively, defined in the western- and eastern-side halves of the meridional *H-surface*, and $E_\theta(, j^-,)$ and $E_\theta(, j^+,)$ are, respectively, defined in the north- and the south-side halves of the latitudinal *H-surface*.

In the present spherical geometry case, as is the case with the staggered grid in Cartesian coordinates (Smith 1996a), the conservative relationship $\nabla \cdot \mathbf{H} = 0$ is satisfied exactly. Due to the divergence theorem, the volume integral of $\nabla \cdot \mathbf{H}$ is represented by the surface integrals of **H** in the spherical staggered grid formulation such as

$$V(i^-, j^-, k^-)\nabla \cdot H$$
$$= S_\phi(i^+, j^-, k^-)H_\phi(i+1, j, k) - S_\phi(i^-, j^-, k^-)H_\phi(i, j, k)$$
$$+ S_\theta(i^-, j^+, k^-)H_\theta(i, j+1, k) - S_\theta(i^-, j^-, k^-)H_\theta(i, j, k)$$
$$+ S_r(i^-, j^-, k^+)H_r(i, j, k+1) - S_r(i^-, j^-, k^-)H_r(i, j, k), \tag{14}$$

where $V(i^-, j^-, k^-)$ denotes a volume of the *E-prism* whose centre is located at the *ijk*th *H-node*. The terms, representing the surface integrals of **H** on the right-hand side of eq. (14), are, respectively, represented by sets of line integrals of **E** with the aid of Faraday's law such as eqs (11)–(13) in discrete form. Thus, the right-hand side of eq. (14) is seen to be identically zero.

From Ohm's law (eq. 3), the **E** field components, e.g. $E_r(i, j, k^-)$ and $E_r(i, j, ^+)$ in eq. (11), are coupled to **J** such that

$$J_r(i, j, k) = \sigma(i, j, k-1)E_r(i, j, k^-)$$
$$= \sigma(i, j, k)E_r(i, j, k^+). \tag{15}$$

Similarly, $E_\phi(i^-, j, k)$ and $E_\phi(i^+, j, k)$ in (12), and $E_\theta(i, j^-, k)$ and $E_\theta(i, j^+, k)$ in (13) are coupled to **J** such that

$$J_\phi(i, j, k) = \sigma(i-1, j, k)E_\phi(i^-, j, k)$$
$$= \sigma(i, j, k)E_\phi(i^+, j, k) \tag{16}$$

and

$$J_\theta(i, j, k) = \sigma(i, j-1, k)E_\theta(i, j^-, k)$$
$$= \sigma(i, j, k)E_\theta(i, j^+, k). \tag{17}$$

Combined with eqs (8), (10), (15) and (17), eq. (11) becomes a second-order difference equation for the ϕ-component of **H** such that

$$\frac{1}{2}\left[\frac{l_r(i^+,j^-,k)}{\sigma(i,j-1,k)}+\frac{l_r(i^+,j^-,k-1)}{\sigma(i,j-1,k-1)}\right]\frac{1}{S_r(i,j-1,k)}$$

$$\times\left[l_\phi(i,j,k)H_\phi(i,j,k)-l_\theta(i+1,j-1,k)H_\theta(i+1,j-1,k)\right.$$

$$\left.-l_\phi(i,j-1,k)H_\phi(i,j-1,k)+l_\theta(i,j-1,k)H_\theta(i,j-1,k)\right]$$

$$+\frac{1}{2}\left[\frac{l_\theta(i^+,j-1,k^-)}{\sigma(i,j-1,k-1)}+\frac{l_\theta(i^+,j,k^-)}{\sigma(i,j,k-1)}\right]\frac{1}{S_\theta(i,j,k-1)}$$

$$\times\left[l_\phi(i,j,k)H_\phi(i,j,k)-l_r(i+1,j,k-1)H_r(i+1,j,k-1)\right.$$

$$\left.-l_\phi(i,j,k-1)H_\phi(i,j,k-1)+l_r(i,j,k-1)H_r(i,j,k-1)\right]$$

$$+\frac{1}{2}\left[\frac{l_r(i^+,j^+,k-1)}{\sigma(i,j,k-1)}+\frac{l_r(i^+,j^+,k)}{\sigma(i,j,k)}\right]\frac{1}{S_r(i,j,k)}$$

$$\times\left[l_\phi(i,j,k)H_\phi(i,j,k)+l_\theta(i+1,j,k)H_\theta(i+1,j,k)\right.$$

$$\left.-l_\phi(i,j+1,k)H_\phi(i,j+1,k)-l_\theta(i,j,k)H_\theta(i,j,k)\right]$$

$$+\frac{1}{2}\left[\frac{l_\theta(i^+,j,k^+)}{\sigma(i,j,k)}+\frac{l_\theta(i^+,j-1,k^+)}{\sigma(i,j-1,k)}\right]\frac{1}{S_\theta(i,j,k)}$$

$$\times\left[l_\phi(i,j,k)H_\phi(i,j,k)+l_r(i+1,j,k)H_r(i+1,j,k)\right.$$

$$\left.-l_\phi(i,j,k+1)H_\phi(i,j,k+1)-l_r(i,j,k)H_r(i,j,k)\right]$$

$$=-i\omega\mu S_\phi(i^+,j^-,k^-)H_\phi(i,j,k). \tag{18}$$

Difference equations for the θ- and r-components of **H** can be obtained with a procedure similar to that described above.

Special attention should be paid to the poles. Since the lengths of the ϕ-component *H-edges* are zero, and also the ϕ-components of the **H** field are not defined at the poles, the difference equations for the ϕ- and θ-components that include H_ϕ at the pole can be assumed to take the same form as e.g. eq. (18). However, since H_r at the pole is determined by all the adjacent H_ϕ and H_θ components surrounding the pole, its difference equation should be written accordingly, for example, for the north pole as follows:

$$\sum_{i=1}^{L}\frac{1}{2}\left[\frac{l_\phi(i,1^+,k^+)}{\sigma(i,1,k)}+\frac{l_\phi(i-1,1^+,k^+)}{\sigma(i-1,1,k)}\right]\frac{1}{S_\phi(i,1,k)}$$

$$\times\left[l_r(1,1,k)H_r(1,1,k)+l_\theta(i,1,k+1)H_\theta(i,1,k+1)\right.$$

$$\left.-l_r(i,2,k)H_r(i,2,k)-l_\theta(i,1,k)H_\theta(i,1,k)\right]$$

$$=-i\omega\mu\left[2\pi r(k^+)^2\{1-\cos\theta(1^+)\}\right]H_r(1,1,k). \tag{19}$$

The second-order difference equations (eqs 18 and 19) can be expressed in matrix form as

$$\begin{bmatrix}\mathbf{A}_{\phi\phi}&\mathbf{A}_{\phi\theta}&\mathbf{A}_{\phi r}\\\mathbf{A}_{\theta\phi}&\mathbf{A}_{\theta\theta}&\mathbf{A}_{\theta r}\\\mathbf{A}_{r\phi}&\mathbf{A}_{r\theta}&\mathbf{A}_{rr}\end{bmatrix}\begin{bmatrix}\mathbf{lH}_\phi\\\mathbf{lH}_\theta\\\mathbf{lH}_r\end{bmatrix}=\begin{bmatrix}\mathbf{lB}_\phi\\\mathbf{lB}_\theta\\\mathbf{lB}_r\end{bmatrix}, \tag{20}$$

where the vector **lH** contains contour integrals to be solved of the **H** field values along their *H-edges*. Since we assign the boundary **H** field values at $r=10r_e$ $[H_{\phi,\theta}(i,j,1)$ with P_1^0 configuration] and in the core $[H_{\phi,\theta}(i,j,N+1), H_r(i,j,N)=0]$, terms including those values in eq. (18) or (19) are moved to the right-hand side of the respective equations as constants, while terms with the *H*-values to be found are moved to the left-hand side. These boundary value terms and zeroes, for the

equations that include no boundary value terms, are contained in the vector **lB**. $\mathbf{A}_{\phi\theta}$ denotes a sub-block of coefficient matrix **A**, and it relates contour integrals of ϕ-component values and θ-component boundary values.

It is noteworthy that the coefficient matrix **A** is symmetric, since **A** relates contour integrals of **H**, rather than the **H** field values themselves. The same symmetry characteristic in **A** was obtained in the Cartesian staggered-grid formulation by Mackie *et al.* (1993) and Smith (1996a). Furthermore, it is obvious that the matrix **A** is sparse and real everywhere except along the diagonal, as was also the case with the previous Cartesian formulation.

3 CONJUGATE GRADIENT METHOD AND $\nabla\cdot\mathbf{H}$ CORRECTION

The significant conductivity contrast between the earth and air leads the coefficient matrix **A** to be ill-conditioned. The typical 1-norm condition number for a model containing a resistive air layer ($\sigma_{air}=10^{-10}$ S m^{-1}) is 10^{13}. This is reduced to 10^5 for an equivalent model with a conductive air layer ($\sigma_{air}=10^{-1}$ S m^{-1}). Effective preconditioning of the matrix system is therefore essential. We employ incomplete Cholesky decomposition of diagonal submatrices $\mathbf{A}_{XX}$ (Mackie & Madden 1993) for this purpose. After preconditioning, for the resistive air layer model, the condition number is reduced to 10^8.

Since the matrix **A** is real everywhere except along the diagonal, Axelsson's (1980; 1994) minimum residual conjugate direction algorithm (MRA) is used to obtain the solution. MRA is an iterative method for finding the solution to real, symmetric and positive-definite systems of equations. The present induction system deviates from the rule requiring real symmetric systems. For the induction problem in Cartesian coordinates, Mackie *et al.*'s (1994) experience had been that this did not appear to be a factor in the relaxation, other than breaking the monotonic convergence property. In order to exploit this desirable property of rapid convergence using MRA, our efforts at deriving a solution to the induction problem in spherical coordinates obliged us to find a solution that did not change the basic structure of the matrix system. Having accomplished this, we found that the MRA method appears to converge rapidly for a spherical earth. Work currently underway (Toh *et al.* 1999) suggests alternative approaches that may accelerate convergence, particularly in parallel computational environments.

As mentioned in the previous section, the conservative relationship $\nabla\cdot\mathbf{H}=0$ should be strictly valid for the **H** fields on the staggered grid, even for the present spherical case. For eq. (14) to hold, the terms involving the products of S and H in that equation should be computed exactly by line integrals of E, as in eqs (11)–(13), or by using the product of S and H as obtained from eq. (18) by dividing both sides of the equation by $-i\omega\mu$. However, after such a division, the orders of the left-hand and right-hand sides of (18) are found to be $O(l_g^2H/(\omega\mu\sigma l_g^2))$ and $O(l_g^2H)$, respectively, where l_g is the representative grid length. Here the product $\omega\mu\sigma l_g^2$ is $\sim10^{-10}$ when $l_g=100$ km, $\sigma=10^{-10}$ S m^{-1} and $T=1$ day. Numerical error can therefore accumulate significantly in the terms involving the products of S and H on the right-hand side of the equation. This may cause a large non-zero divergence in the solution. The effect of this is to introduce into the exact solution the fields of an assortment of spurious magnetic monopoles, and

this situation worsens the convergence property of the MRA relaxation. In order to alleviate this, the divergence $\Psi = \nabla \cdot \mathbf{H}$ is eliminated at a given set of MRA relaxations by solving for the potential Φ that satisfies

$$\nabla \cdot \nabla \Phi = \Psi \qquad (21)$$

following Mackie *et al.* (1994) and Smith (1996b). Once we have obtained Ψ, the $\mathbf{H}$ field can be updated via $\mathbf{H}_{new} = \mathbf{H}_{old} - \nabla \Psi$ without changing the resulting $\mathbf{E}$ fields, since the relationship

$$\nabla \times (\mathbf{H} - \nabla \Psi) = \nabla \times \mathbf{H} = \mathbf{J} \qquad (22)$$

is also strictly valid on the staggered grid. The discrete version of eq. (21) is solved using the MRA and an incomplete Cholesky decomposition as a preconditioner. A few relaxation steps are required in obtaining Ψ in order to improve greatly the convergence of the main MRA relaxation for eq. (20).

In Fig. 2 we compare the convergence property of the MRA relaxations for the same model (a double-hemisphere model that will be described in the next section) with and without the $\nabla \cdot \mathbf{H}$ correction. Fig. 2 shows, for each relaxation step, the normalized residual ΔlB and the normalized change of the
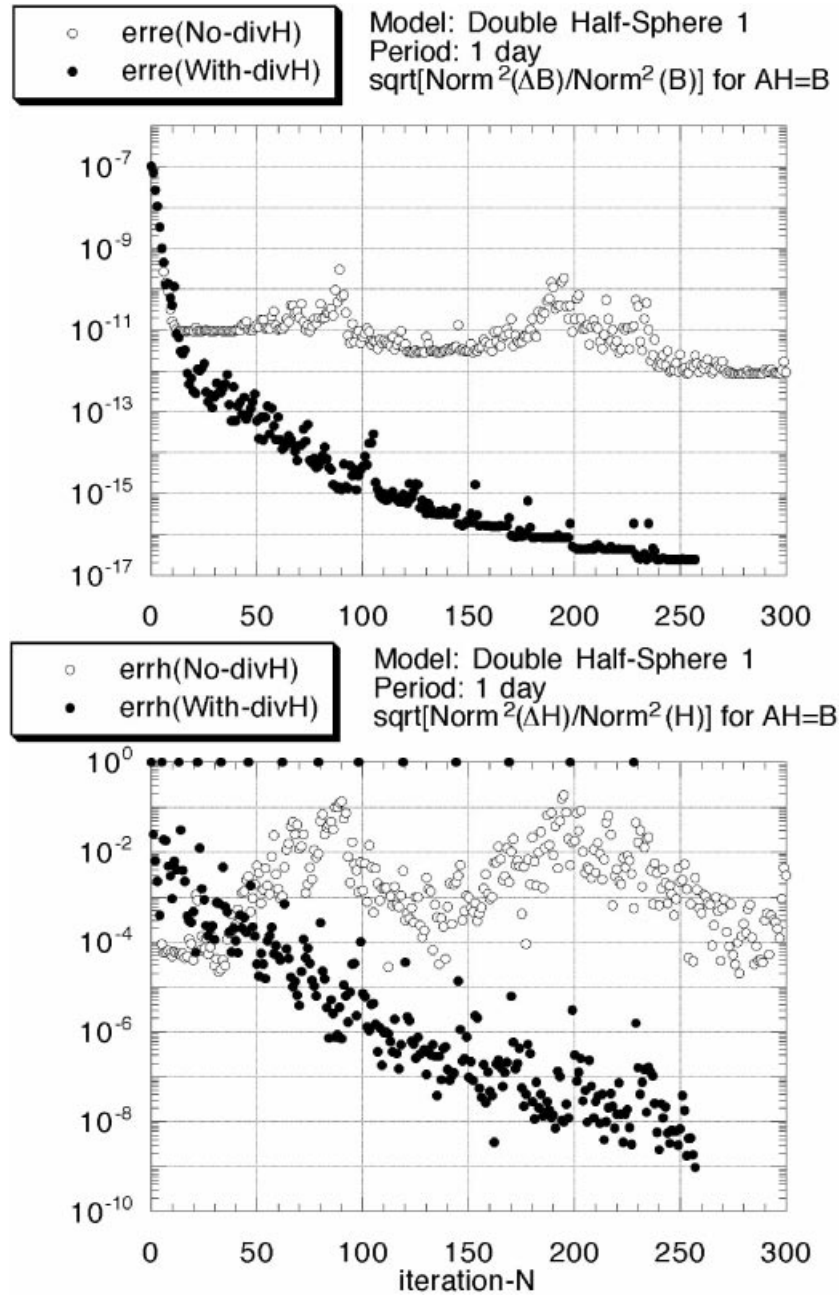
Figure 2. Comparison of the convergence property of the MRA relaxations for the same model (a double-hemisphere model as described in Section 4) with and without the $\nabla \cdot \mathbf{H}$ correction. (top) The normalized residual ΔlB (eq. 23) and (bottom) the normalized change of the solution ΔlH (eq. 24) at each relaxation step are shown. Open circles denote relaxation without the $\nabla \cdot \mathbf{H}$ correction and closed circles denote that with the correction. At times with the corrections, closed circles are plotted at the 10^0 level in the bottom panel.

solution $\Delta l\mathbf{H}$,

$$\Delta l\mathbf{B} = l\mathbf{B} - A l\mathbf{H}\,, \tag{23}$$

$$\Delta l\mathbf{B} = \mathbf{H}_{\text{new}} - \mathbf{H}_{\text{old}}\,. \tag{24}$$

In both parts of Fig. 2, open circles denote relaxations without the $\nabla \cdot \mathbf{H}$ correction, and closed circles denote those with the correction. The MRA iteration numbers at which divergence corrections were made are indicated in Fig. 2(b) by closed circles plotted at the 10° level.

Rapid convergence is seen, with a decrease in error of five orders of magnitude in the first 20 iterations for $\Delta l\mathbf{B}$ and a decrease of three orders of magnitude for $\Delta l\mathbf{H}$. The convergence slows gradually for subsequent iterations. Although without divergence correction, only minor improvements with significant fluctuations in $\Delta l\mathbf{B}$ are detected after 10 iterations, $\Delta l\mathbf{B}$ converges progressively (but not monotonically) when divergence corrections are applied. The quantity $\Delta l\mathbf{H}$ converges to $< 10^{-9}$ (which we have taken to be the stopping criterion). The divergence correction plays a significant role in accelerating convergence for $\Delta l\mathbf{H}$.

4 COMPARISONS WITH OTHER NUMERICAL AND QUASI-ANALYTICAL SOLUTIONS

Before attempting to model electromagnetic induction in an earth with realistic electrical structure, it is prudent to verify the present staggered-grid finite difference (SGFD) approach against other solutions to the forward problem. In this paper, we check our results against other numerical and quasi-analytical solutions that employ entirely different methods of solution. The checks are restricted to the P_1^0 source structure.

4.1 Azimuthally symmetric cross-comparison

The first check is against the azimuthally symmetric, double-hemisphere thin shell model shown in Fig. 3. The thin shell is buried at a depth of 400 km ($r = 5971$ km) in a background radially symmetric earth. The intent of validating the present solution by using such a model is to test the accuracy of this solver for models containing heterogeneous structure in the mid-mantle. Such depths are associated with the highest resolving power for external induction data due to the relaxation phase of D_{st} variations (e.g. Schultz 1990).

The shell is divided at the equator into two hemispherical sections. The northern hemisphere shell is a good conductor with conductance $\tau = 4 \times 10^4$ S. The southern shell is more resistive, with $\tau = 2 \times 10^3$ S. The conductivity of the background 1-D structure is 2.5×10^{-3} S m^{-1}, down to a depth of 800 km, and 2.5 S m^{-1} beneath this depth. Kuvshinov & Pankratov (1994) have made available a numerical solution for the global induction problem for the buried shell (BS) model using an integral equation formulation (Singer & Fainberg 1985; Fainberg *et al.* 1993). The solution exploits the modified iterative–dissipative method of Singer (1995) to solve an integral equation. The method is based on a Neumann series expansion, which always converges, even for extremely large conductivity contrasts. The BS model comprises an inhomogeneous thin spherical sheet embedded at a given depth within a radially symmetric medium. A. Kuvshinov has kindly provided us with responses for such a model, to an external P_1^0 source, for the period $T = 1$ day.
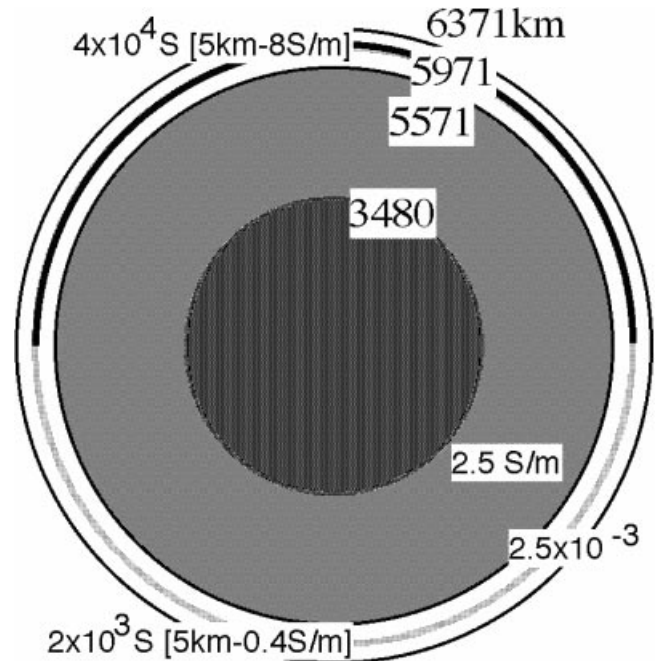

Figure 3. A sketch of the azimuthally symmetric, double-hemisphere thin shell model.

Since we cannot model infinitesimally thin conducting shells with finite-sized curved prisms, we model the thin sheet as a 5-km-thick shell, centred at 400 km depth. The northern shell has a conductivity of 8.0 S m^{-1}, and the southern shell 0.4 S m^{-1}. Consequently, the overall conductance τ is the same in both models. For zonal external source excitation (e.g. P_1^0), such an azimuthally symmetric conductivity structure produces azimuthally symmetric secondary fields. Given the longitudinal invariance of the fields for the present case, the division number L in the ϕ-direction was set to 2. In the θ-direction, the computational domain was divided evenly into 36 facets, with a grid spacing of 5°.

In Fig. 4 we show the two non-zero components of $\mathbf{H}$ and the one non-zero component of $\mathbf{E}$ as a function of geomagnetic colatitude. The BS results are shown as solid curves and the results of the SGFD code as filled symbols. In the model, the external source produces a southward horizontal field of 100 nT at the equator. The in-phase part of the internal induced field increases this to about 140 nT above the more conductive half-shell, and to only 120 nT above the less conductive half-shell. Similarly, H_r is reduced by induction from ± 100 nT at the N and S poles to $+22$ nT and -34 nT, respectively. Radial mesh divisions for the respective computations were 50, 67 and 136 including the air layer. For the largest computation [i.e. $(L, M, N) = (2, 36\,136)$], 11.7 Mbyte of memory was required, and it took 60 s to obtain the one-period solution on a single 333 MHz Digital Alpha® EV56 processor (0.6 GFLOP peak speed). The percentage deviation between the SGFD solution and the BS solution is also shown for each of the field components. The difference between these two sets of solutions is small (generally <1 per cent) except within $\pm 20^{\circ}$ of the geomagnetic equator, which here is the boundary between the two hemispherical thin shells. For this model, the spatial gradients in the fields are greatest at the
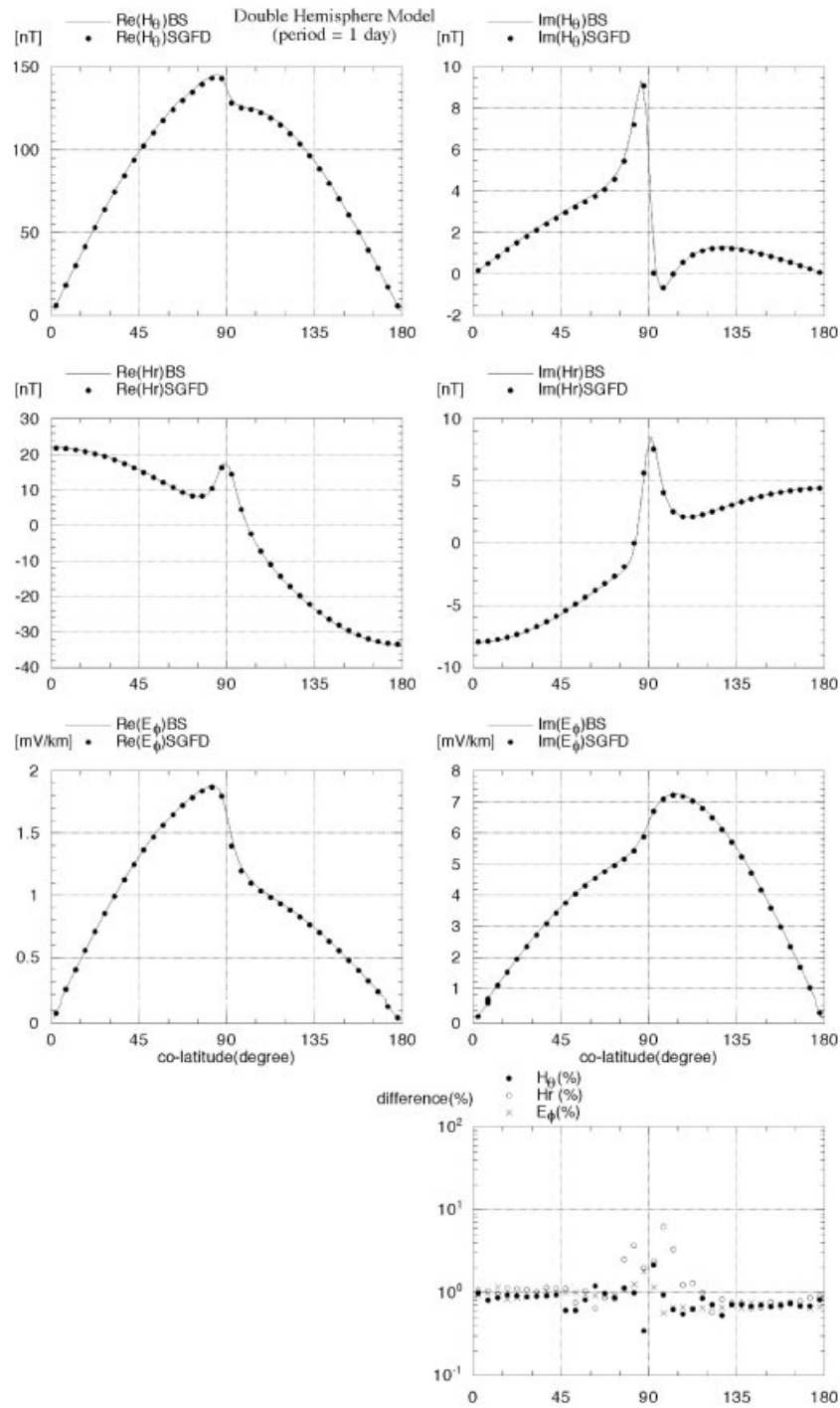
Figure 4. Results of the comparison between the SGFD solution and the BS solution for the double-hemisphere model shown in Fig. 3. The two non-zero components of **H** in nT and the one non-zero component of **E** in mV km^{-1} are shown as functions of geomagnetic colatitude (real components on the left-hand side, imaginary on the right). The BS results appear as solid curves, and the SGFD results as filled symbols. The bottom right-hand panel illustrates the percentage deviation of the SGFD solution relative to the BS solution. Accuracies of better than 1 per cent in the fields are seen for regions distant from the equatorial hemispheric boundary separating the two conductivity domains.

equator. The SGFD and BS solutions employed different computational grids. This makes it difficult to carry out direct comparisons between the solutions in this region.

In Fig. 5 we show the magnetotelluric (MT) impedances ($Z_{\phi\theta} = E_\phi/H_\theta$) in terms of apparent resistivity and phase. Also shown is the complex Geomagnetic Deep Sounding (GDS) transfer function ($Z_{r\theta} = H_r/H_\theta$). Three sets of results are shown,

representing, respectively, radial discretization levels of 0.25, 1 and 4 nodes per skin depth. For the finest radial mesh spacing, the discrepancy between the SGFD- and BS-calculated responses is exceedingly small. The inflection in the GDS response near the equator, as well as the difference between the northern and southern hemispheres, is well reproduced by the SGFD method.

4.2 Azimuthally asymmetric cross-comparison

Martinec (1998) recently developed a semi-analytic method to obtain a solution of the electromagnetic induction problem
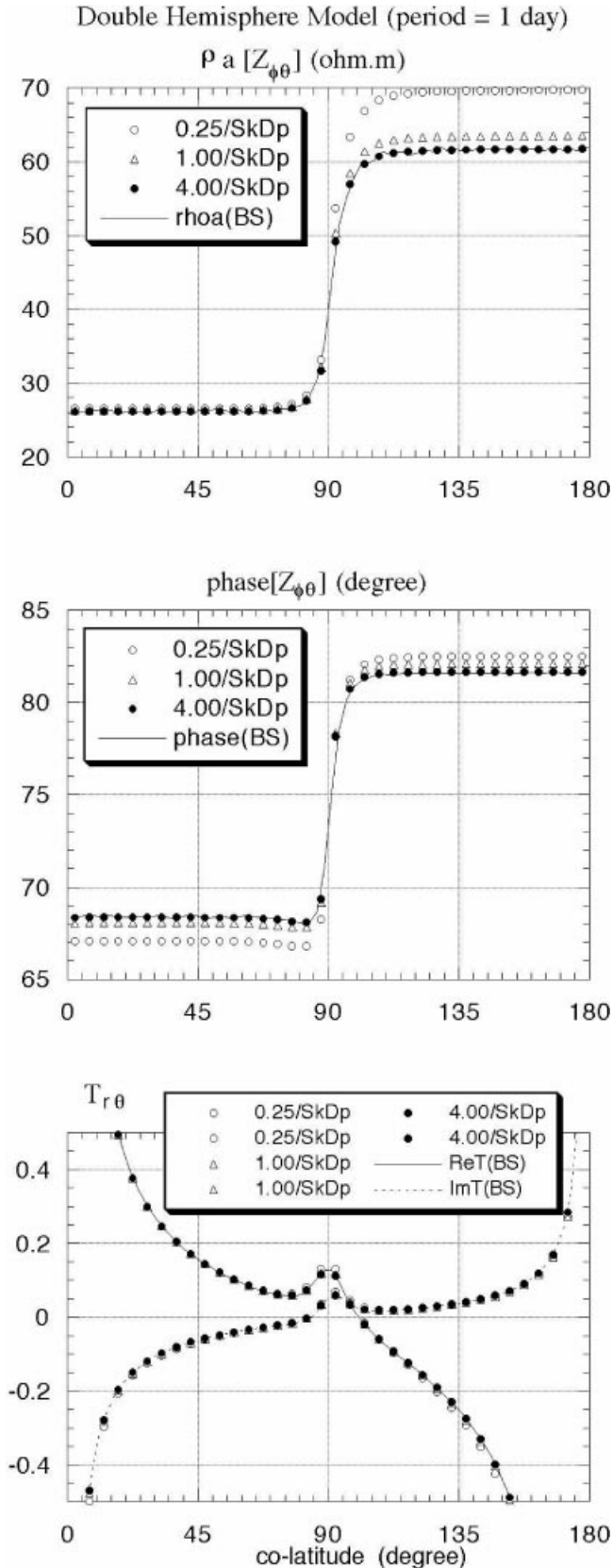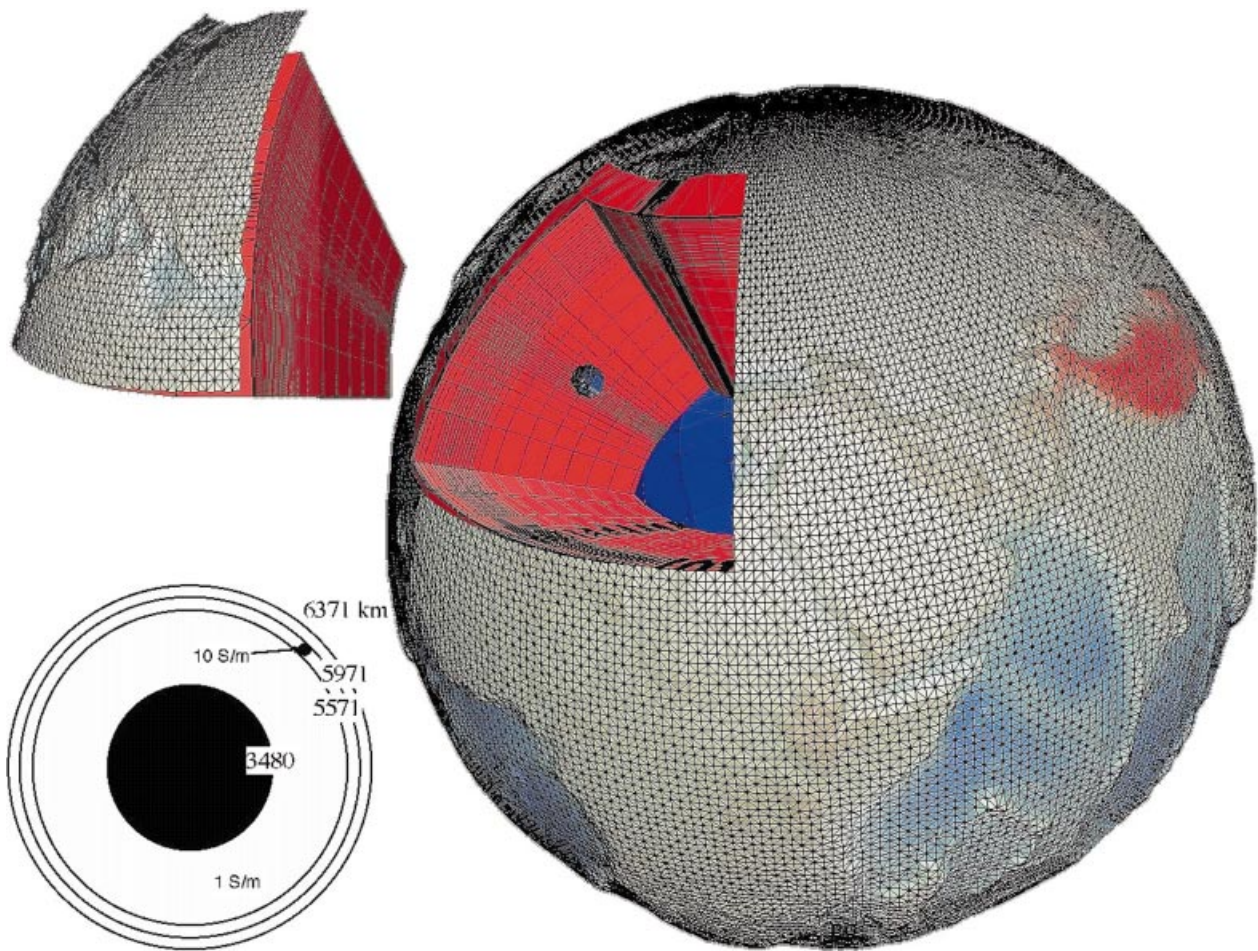

Figure 5. Results of the comparison between the SGFD solution and the BS solution for the double-hemisphere model shown in Fig. 3. The surface values of the magnetotelluric (MT) impedance ($Z_{\phi\theta} = E_\phi/H_\theta$), scaled into apparent resistivity in Ω m and phase in degrees, and the real and imaginary parts of the Geomagnetic Deep Sounding (GDS) transfer functions ($T_{r\theta} = H_r/H_\theta$) are shown versus geomagnetic colatitude (from top to bottom). The solid curves are the BS results. Open circles, open triangles and closed circles denote the SGFD results, with the minimum number of radial nodes per skin depth set to 0.25, 1.0 and 4.0, respectively.

for an earth comprising azimuthally asymmetric eccentrically nested spheres. The method is an extension of Everett & Schultz's (1995) solution for axisymmetric eccentrically nested spheres. The axisymmetric solution had been used previously to partially validate the Everett & Schultz (1996) finite element forward solver. This validation was restricted in that fully 3-D models that generate axially asymmetric fields could not be tested. Martinec's solution eliminates this restriction, and is used here to validate the SGFD method. Such a model is sketched in Fig. 6: a small sphere with a radius of 200 km and electrical conductivity of $10 \, \mathrm{S \, m^{-1}}$ is buried at a depth of 600 km in a uniform $1 \, \mathrm{S \, m^{-1}}$ earth. The centre of the embedded sphere is located at $(r, \theta, \phi) = (5771 \, \mathrm{km}, 45°, 0°)$. This model is representative of one class of geodynamical targets, a discrete conductive or resistive body located in the mid-mantle. The external source field is also set to have P_1^0 form for this model.

A significant difference between this class of the model and those considered previously is that, even with axially symmetric (zonal) source current excitation, eddy currents are forced across and around the electrical conductivity interface, producing strong galvanic effects. Z. Martinec has kindly provided us with responses for a $T \sim 24$ day period ($\omega = 3 \times 10^{-6}$) estimated by using spherical harmonic expansion of up to degree 18. The infinitely conducting core used in the SGFD solution could not be included in this nested sphere model computation. The effects of the absence of the core beneath $r = 3480$ km can be neglected in the induced fields near the model earth's surface, since the skin depth for this period is 728 km in a homogeneous earth with $1 \, \mathrm{S \, m^{-1}}$ conductivity.

For the nested sphere model, we computed responses for the SGFD solver with $(L, M, N) = (50, 31, 53)$ mesh division. In this computation, a curved rectangular prism just enveloping the conductive small sphere is divided into $8 \times 8 \times 8$ prisms whose grid spacing is 0.5° in the ϕ- and θ-directions and 50 km in the r-direction. Latitudinal and longitudinal mesh divisions are gradually enlarged up to 20° as their positions grow more distant from the inclusion. The non-uniform mesh divisions are illustrated in Fig. 6. A minimum of four radial nodes per skin depth was maintained throughout the computational domain. This computation required 99.5 Mbyte memory and 3041 s computation time on a single 625 MHz Digital Alpha® EV56 processor (1.2 GFLOP peak speed). To ensure convergence, the MRA relaxation was continued until the normalized change of the solution (eq. 16) was $< 10^{-11}$.

The radial dependence of the percentage deviation between the SGFD solution and the nested sphere analytic solution (NS) is shown in Fig. 7. Here, the three components of **H** beneath the earth's surface at $(\phi, \theta) = (0°, 50°)$ are displayed as solid curves. Since H_ϕ at $\phi = 0°$ should be identically zero due to the symmetry of the problem, we show only differences

Figure 6. Schematic of an azimuthally asymmetric, eccentrically nested sphere model. The SGFD computational grid is shown as a series of gridlines of increasing sampling frequency as the embedded conductive spherical anomaly (shown as a small blue sphere) is approached. The vertically exaggerated geographical reference on the surface of the model earth is provided for scale and has no other significance.
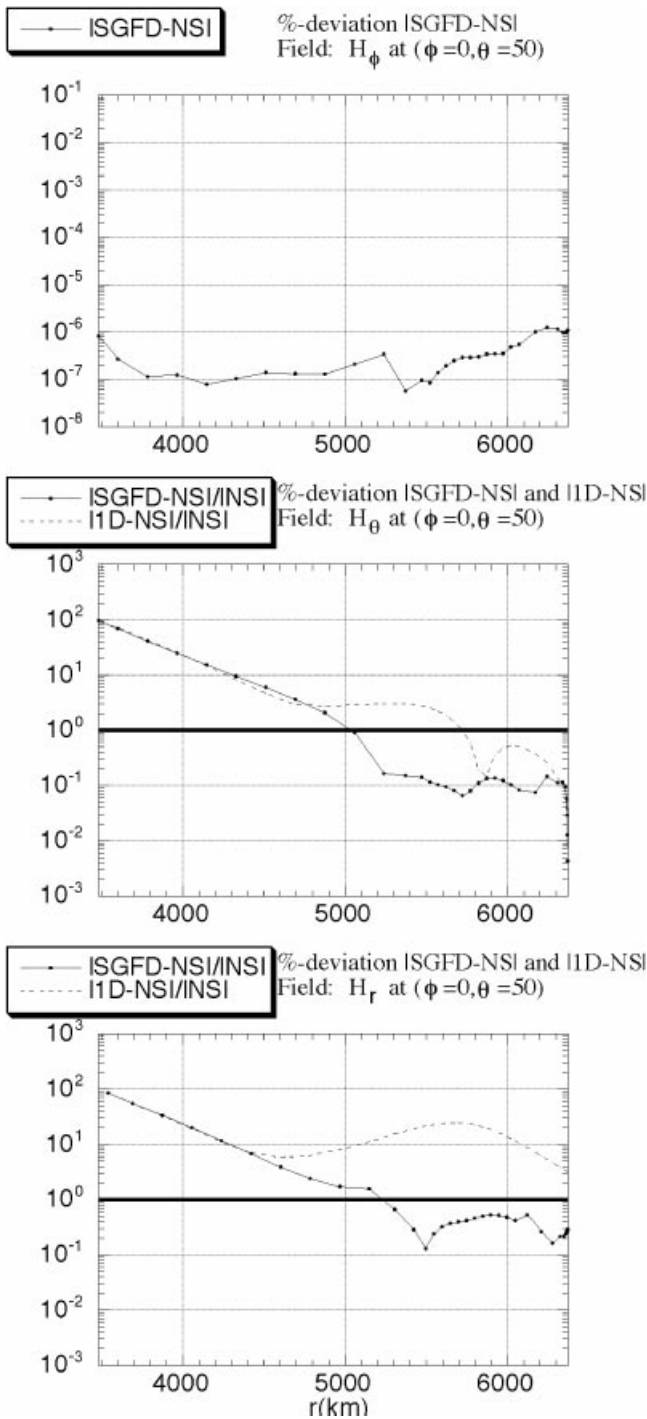
between the SGFD solution and the NS solution (amplified by a factor of 100) for H_ϕ. In order to evaluate the results for H_θ and H_r, the 1-D analytic solution without the small spherical inclusion, and with a 3480-km-radius infinitely conductive core is also compared with the NS solution. The purpose of the 1-D calculations is both to examine the effect of the 10 S m^{-1} spherical inclusion and to test the effect of a perfectly conducting core at 3480 km upon the semi-analytic NS solution. This is shown by dashed curves in the figure. The solutions are normalized such that all the H_θ values at the surface, i.e. $(\phi, \theta, r) = (0°, 50°, 6371 \text{ km})$, are identical for the different solutions. Therefore, the deviation of H_θ at the surface is set to be zero, whereas H_θ at any other position, as well as H_ϕ and H_r for any given solution, can be different from those for any other solution.

The expected value of zero for the H_ϕ component is approximated accurately, with computed values between 10^{-8} and 10^{-9}. Remarkable agreement (within 1 per cent) between the SGFD and NS solutions is obtained for the H_θ and H_r components in the region shallower than $r = 5000$ km, whereas the deviation of the 1-D solution remains at the 1 per cent level for the H_θ component and the 10 per cent level for the H_r component. Since the infinitely conductive core is not included in the NS solution, the deviation grows significantly

towards the CMB. However, this effect can be neglected in the shallower parts of the model, as mentioned previously.

The real part of the response function H_ϕ/H_θ on the model earth's surface, calculated by the SGFD method, is displayed in the top part of Fig. 8. If the earth had uniform conductivity under an axially symmetric source current (e.g. P_1^0 source), induced current would flow purely eastwards and no H_ϕ component would arise. The effect of current channelling in the vicinity of the conductive spherical anomaly generates a quadrupole-like pattern in the surface field. In the first and third lobes of this pattern the response function takes on a positive value. This is due to the northward diversion of the induced currents around the anomaly. The situation is reversed in the remaining two lobes. These results may be compared against the quasi-analytical embedded spheres computation in the bottom part of the figure.

Whilst the quasi-analytical method has the potential of yielding a result of asymptotically analytical accuracy, it does rely on numerical approximations. This has the practical effect of limiting the accuracy of this solution. Z. Martinec computed the quasi-analytical responses by using a degree 18 spherical harmonic expansion. In Fig. 8 we compare the degree 18 expansion nested spheres result with a similar result obtained for an expansion truncated at degree 10. A quadrupole

Figure 7. The radial dependence of the percentage deviation between the SGFD solution and the nested sphere quasi-analytic solution (NS) for three components of **H** beneath the earth's surface at $(\phi, \theta) = (0°, 50°)$ (solid lines). For the H_ϕ component, we show the difference between the SGFD and the NS solutions (multiplied by a factor of 100). This component should be identically zero. For the components H_θ and H_r, the 1-D analytic solution without the small spherical inclusion, but with a 3480 km infinitely conductive core is compared with the NS solution (dashed curve). Here, the solutions are normalized so that all the H_θ values at the surface, i.e. $(\phi, \theta, r) = (0°, 50°, 6371 \text{ km})$, are identical for the different solutions. Remarkable agreement to better than the 1 per cent level is seen between the SGFD and NS solutions for the H_θ and H_r components for the model region shallower than 5000 km.
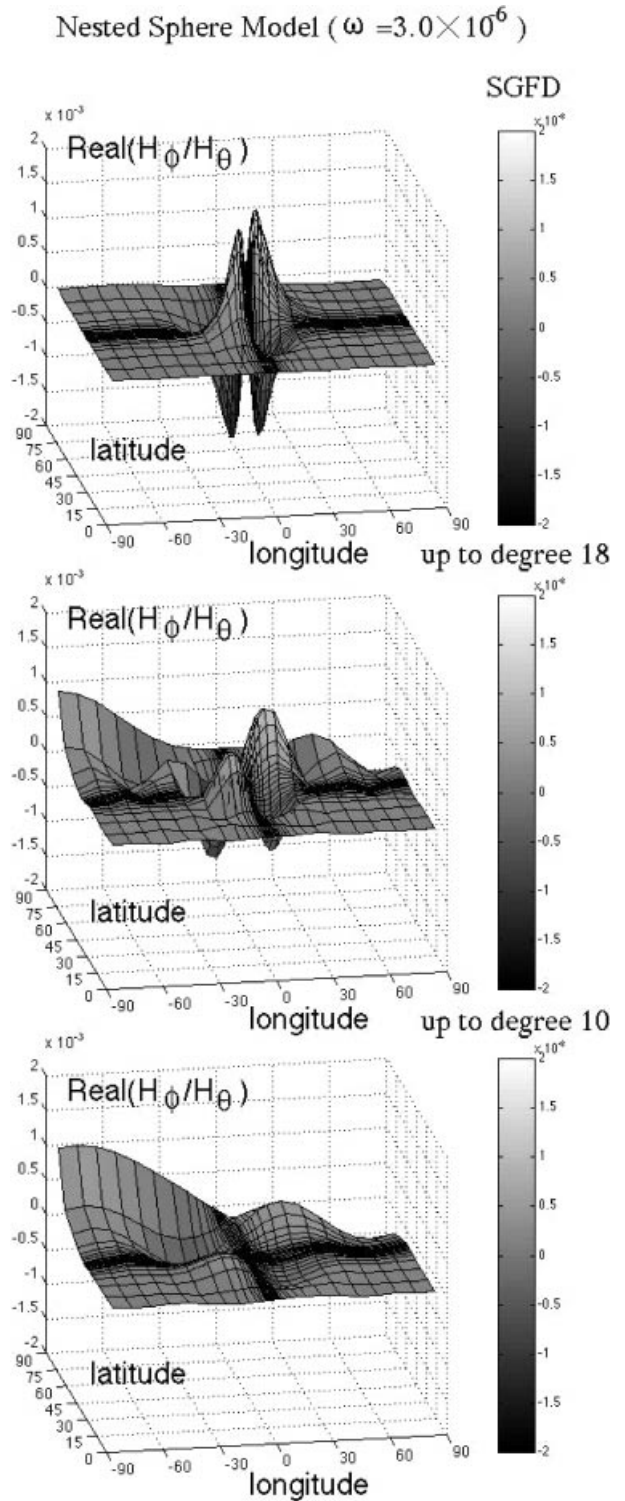
Figure 8. The real part of the response function H_ϕ/H_θ on the model earth's surface, calculated by the SGFD method (top), the NS quasi-analytical solution by using a degree 18 spherical harmonic expansion (middle) and that truncated at degree 10 (bottom). The effect of current channelling in the vicinity of the conductive spherical anomaly generates a quadrupole-like pattern in the surface field. The intensity of the anomaly is somewhat enhanced, and the width of the anomaly's peak is narrower for the SGFD result than for the quasi-analytical solution. For the Martinec calculation, however, peak intensity grows significantly and its width grows narrower as the maximum degree increases from 10 to 18.

surface field pattern similar to that shown previously for the SGFD calculation is seen here. The intensity of the anomaly is somewhat enhanced, and the width of the anomaly's peak is narrower for the SGFD result than for the quasi-analytical solution. For the Martinec calculation, however, peak intensity grows significantly and its width grows narrower as the maximum degree increases from 10 to 18. In the degree 18 quasi-analytical solution, some fluctuations are still detected outside the quadrupole lobes. The wavenumber spectrum of the quasi-analytical solution spherical harmonic coefficients shows that the spectrum is approximately white up to degree 18. Therefore, a degree 18 expansion is probably insufficient for representing the spatial distribution of the fields for the present model. This illustrates the practical limitations of validating the absolute accuracy of competing solution methods. Thus far, our computation cannot be verified to analytical accuracy against the present nested sphere model. By considering the peak growth detected in the semi-analytic solution as the degree of spherical harmonic expansion increases, the present result suggests good correspondence between the SGFD and quasi-analytical methods. Work in progress on the detailed intercomparison of the various methods for solving the 3-D forward problem will address this issue in more detail.

5   CONCLUSIONS

We have developed a staggered-grid finite difference method to compute the electromagnetic induction response of an arbitrary 3-D conducting sphere by external current excitation. This method is appropriate as the forward solution for the problem of determining the electrical conductivity of the earth's deep interior. The difference equations that we solve are second order in the magnetic field $\mathbf{H}$, and are derived from the integral form of Maxwell's equations on a staggered grid in spherical coordinates. This is an outgrowth of a method originally developed by Mackie *et al.* (1994) for Cartesian geometry. The resulting matrix system of equations possesses the same general structure as that for Mackie's Cartesian case—the matrix is sparse, symmetric, real everywhere except along the diagonal, and ill-conditioned. The system is solved using the minimum residual conjugate gradient method with preconditioning by incomplete Cholesky decomposition of the diagonal sub-blocks of the coefficient matrix. In order to ensure that there is zero $\mathbf{H}$ divergence in the solution, corrections are periodically made to the $\mathbf{H}$ field during the relaxation phase of the solution.

After comparison between an integral equation solution (BS) by Kuvshinov & Pankratov (1994) and the SGFD solution for an azimuthally symmetric, buried thin double-hemisphere model, we found that SGFD demonstrated excellent asymptotic convergence to the BS solution as mesh division was refined. We also computed responses for an azimuthally asymmetric configuration of eccentrically nested spheres. Along the meridian of longitude centred on the conductive anomaly, the SGFD and spherical harmonic degree 18 quasi-analytical solution showed extremely good correspondence, with less than a 1 per cent difference in the surface value of H_r, and significantly smaller differences in the two horizontal components of H at the surface. The embedded spherical anomaly in the model was very small (with a radius of 200 km), and we found that the degree 10 and degree 18 quasi-analytical solutions of Martinec (1998) were likely truncated at too low a spherical harmonic degree to represent the spatial distribution of the

fields accurately everywhere on the model earth's surface. As a result, the SGFD and quasi-analytical staggered-grid solutions cannot yet be compared with accuracy everywhere on the model surface. The two solutions do show excellent agreement in the spatial distribution of the responses, and the SGFD results were in the direction of convergence (versus spherical harmonic degree) of the quasi-analytical solution.

REFERENCES

Abramowitz, M. & Stegun, I.A., 1965. *Handbook of Mathematical Functions,* Dover, New York.

Axelsson, O., 1980. Conjugate gradient type methods for unsymmetric and inconsistent systems of linear equations, *Linear Algebra and its Appl.,* **29,** 1–16.

Axelsson, O., 1994. *Iterative Solution Methods,* Cambridge University Press, Cambridge.

Bai, Q. & Kohlstedt, D.L., 1993. Effects of chemical environment of the solubility and incorporation mechanism for hydrogen in olivine, *Phys. Chem. Min.,* **19,** 460–471.

Banks, R.J., 1969. Geomagnetic variations and the electrical conductivity of the upper mantle, *Geophys. J. R. astr. Soc.,* **266,** 123–192.

Bahr, K., Olsen, N. & Shankland, T.J., 1993. On the combination of the magnetotelluric and the geomagnetic depthsounding method for resolving an electrical conductivity increase at 400 km depth, *Geophys. Res. Lett.,* **20,** 2937.

Egbert, G. & Booker, J.R., 1992. Very long period magnetotellurics at Tucson observatory: implications for mantle conductivity, *J. geophys. Res.,* **97**(B11), 15 099–15 112.

Egbert, G., Booker, J.R. & Schultz, A., 1992. Very long period magnetotellurics at Tucson observatory: estimation of impedances, *J. geophys. Res.,* **97**(B11), 15 113–15 128.

Everett, M.E. & Schultz, A., 1995. Geomagnetic induction in eccentrically nested spheres, *Phys. Earth planet. Inter.,* **92,** 189–198.

Everett, M.E. & Schultz, A., 1996. Geomagnetic induction in a heterogeneous sphere: azimuthally symmetric test computations and the response of an undulating 660-km discontinuity, *J. geophys. Res.,* **101,** 2765–2783.

Fainberg, E.B., Pankratov, O.V. & Singer, B.S., 1993. Thin sheet modelling of surface and deep inhomogeneities, *Geophys. J. Int.,* **113,** 144–154.

Fujii, I., Utada, H. & Yumoto, K., 1995. Averaged distribution of electrical conductivity of the Philippine Sea Plate, *IUGG, XXI General Assembly, Week B, Abstracts,* **21,** 63–64.

Fujii, I. & Schultz, A., 1998. The sensitivity of mantle electrical modelling to the spatial distribution of the global magnetic observatory system—a new requirement for an old network, *EOS, Trans. Am. geophys. Un.,* Suppl., **79**, F64.

Hirsch, L.M. & Shankland, T.J., 1993. Quantitative olivine-defect chemical model: insights on electrical conduction, diffusion and the role of Fe content, *Geophys. J. Int.,* **114**, 21–35.

Hirsch, L.M., Shankland, T.J. & Duba, A.G., 1993. Electrical conduction and polaron mobility in Fe-bearing olivine, *Geophys. J. Int.,* **114**, 36–44.

Karato, S., 1990. The role of hydrogen in the electrical conductivity of the upper mantle, *Nature,* **347**, 272–273.

Koyama, T. & Utada, H., 1998. Induction modelling in the 3D global Earth—modified Neumann Series, *Proc. Conductivity Anomaly Symp,* 279–286 (in Japanese).

Kuvshinov, A.V. & Pankratov, O.V., 1994. Electromagnetic induction in a spherical Earth with inhomogeneous conducting mantle: thin sheet forward problem, *Proc. 12th Workshop on the Earth, Brest, France,* 83.

Kuvshinov, A.V., Avdeev, D.B. & Pankratov, O.V., 1998. Electromagnetic modelling in a spherical Earth with surface and deep conducting inhomogeneities: multi-shell solution, *14th Workshop on Electromagnetic Induction in the Earth, Sinaia, Romania, Abstracts,* 129–130.

Lizarralde, D., Chave, A., Hirth, G. & Schultz, A., 1995. Long period magnetotelluric study using Hawaii-to-California submarine cable data: implications for mantle conductivity, *J. geophys. Res.,* **100**(B9), 17 873–17 854.

Lahiri, B.N. & Price, A.T., 1939. Electromagnetic induction in non-uniform conductors, and the determination of the conductivity of the Earth from terrestrial magnetic variations, *Phil. Trans. R. Soc. Lond.,* A**237**, 509–540.

Mackie, R.L. & Madden, T.R., 1993. Conjugate direction relaxation solutions for 3-D magnetotelluric modeling, *Geophysics,* **58**, 1052–1057.

Mackie, R.L., Madden, T.R. & Wannamaker, P.E., 1993. Three-dimensional magnetotelluric modeling using difference equations–theory and comparisons to integral equation solutions, *Geophysics,* **58**, 215–226.

Mackie, R.L., Smith, J.T & Madden, T.R., 1994. Three-dimensional electromagnetic modeling using finite difference equations: the magnetotelluric example, *Radio Sci.,* **29**, 923–935.

Martinec, Z., 1998. Geomagnetic induction in multiple eccentrically nested spheres, *Geophys. J. Int.,* **132**, 96–110.

Martinec, Z., 1999. Spectral-finite element approach to three-dimensional electromagnetic induction in a spherical Earth, *Geophys. J. Int.,* **136**, 229–250.

Olsen, N., 1998. The electrical conductivity of the mantle beneath Europe derived from C-responses from 3 to 720 hr, *Geophys. J. Int.,* **133**, 298–308.

Olsen, N., 1999. Long-period (30 days–1 year) electromagnetic sounding and the electrical conductivity of the lower mantle beneath Europe, *Geophys. J. Int.,* **138**, 179–187.

Rokityansky, I.I., 1982. *Geoelectromagnetic Investigation of the Earth's Crust and Mantle,* Springer-Verlag, Berlin.

Schultz, A., 1990. On the vertical gradient and lateral heterogeneity in midmantle electrical conductivity, *Phys. Earth planet. Inter.,* **64**, 68–86.

Schultz, A. & Larsen, J.C., 1987. On the electrical conductivity of the mid-mantle, 1–calculation of equivalent scalar magnetotelluric response functions, *Geophys. J. R. astr. Soc.,* **88**, 733–762.

Schultz, A. & Larsen, J.C., 1990. On the electrical conductivity of the mid-mantle, 2–delineation of heterogeneity by application of extremal inverse solutions, *Geophys. J. Int.,* **101**, 565–580.

Schultz, A., Kurtz, R.D., Chave, A.D. & Jones, A.G., 1993. Conductivity discontinuities in the upper mantle beneath a stable craton, *Geophys. Res. Lett.,* **20**, 2941–2944.

Schultz, A. & Pritchard, G., 1998. A three-dimensional inversion for large-scale structure in a spherical domain, in *Three-Dimensional Electromagnetics, Geophysical Developments Series,* pp. 451–476, eds Spies, B. & Oristigliano, M., SEG, Tulsa.

Schultz, A., Semenov, V.Yu., 1993. Modelirovanie Strykturi elektroprovodnosti mantii zemli (Modelling the electrical conductivity structure of the Earth's mantle), *Phyzika Zemli* (*Phys. Earth Russian Acad. Sci.*)*,* **10**, 39–44 (in Russian).

Schultz, A. & Zhang, T.S., 1994. Regularised spherical harmonic analysis and the three dimensional electromagnetic response of the Earth, *Geophys. J. Int.,* **116**, 141–156.

Shankland, T.J. & Duba, A.G., 1997. Correlation of olivine electrical conductivity change with water, *EOS, Trans. Am. geophys. Un.,* **78**, 46.

Shankland, T.J., Peyronneau, J. & Poirier, J.P., 1993. Electrical conductivity of the Earth's lower mantle, *Nature,* **366**, 453–455.

Singer, B.Sh., 1995. Method for solution of Maxwell's equations in non-uniform media, *Geophys. J. Int.,* **120**, 590–598.

Singer, B.Sh. & Fainberg, E.B., 1985. *Electromagnetic Induction in Non-Uniform Thin Sheets and Shells,* IZMIRAN, Moscow (in Russian).

Smith, J.T., 1996a. Conservative modeling of 3-D electromagnetic fields, Part 1: properties and error analysis, *Geophysics,* **61**, 1308–1318.

Smith, J.T., 1996b. Conservative modeling of 3-D electromagnetic fields, Part 2: biconjugate gradient solution and an accelerator, *Geophysics,* **61**, 1319–1324.

Tarits, P., Wahr, J. & Lognonné, P., 1999. Influence of conductivity heterogeneities at and near the core–mantle boundary on the geomagnetic secular variation, *Geophys. J. Int.,* submitted.

Toh, H., Schultz, A. & Uyeshima, M., 1999. Biconjugate gradient solution of a spherical 3D EM forward solver using staggered-grid integral formulation and its acceleration over multi-frequencies, *Int. Symp. in 3-D Electromagnetic Modeling (3DEM-2), Oct. 27–29,* University of Utah, Salt Lake City (extended abstract).

Xu, Y., Poe, B.T., Shankland, T.J. & Rubie, D.C., 1998a. Electrical conductivity of olivine, wadsleyite, and ringwoodite under upper-mantle conditions, *Science,* **280**, 1415–1419.

Xu, Y., McCammon, C. & Poe, B.T., 1998b. The effect of alumina on the electrical conductivity of silicate perovskite, *Science,* **282**, 922–924.

Zhang, T.S. & Schultz, A., 1992. A three-dimensional perturbation solution for the EM induction problem in a spherical Earth—the forward problem, *Geophys. J. Int.,* **111**, 319–334.

APPENDIX A: EFFECT OF NON-ZERO AIR CONDUCTIVITY

The accuracy of the forward solution is seen to be relatively insensitive to the chosen value of air conductivity, and to the distance at which we set the Dirichlet boundary (e.g. $10r_e$). We compare the case where Laplace's equation is satisfied exactly (that is, an air layer of zero conductivity) with the situation where the Helmholtz equation is satisfied for very low but non-zero-conductivity air layers.

Consider analytical solutions of the Helmholtz equation (1)–(3) for the dependence of the **H** field with radial distance from the earth. For the radial component, these solutions are $r^{-1}j_l(z)$ and $r^{-1}y_l(z)$, and for the tangential component, $r^{-1}[j_l(z) + z(dj_l(z)/dz)]$ and $r^{-1}[y_l(z) + z(dy_l(z)/dz)]$. Here r, l, j_l, y_l and z represent, respectively, the distance from the earth's centre, the degree of spherical harmonic, the spherical Bessel functions of degree l of the first and second kinds and $z = kr$, with $k = \sqrt{-i\omega\mu\sigma}$. Here, $r^{-1}j_l(z)$ and $r^{-1}y_l(z)$ can be expanded

as

$$r^{-1} j_l(z) = A_0^{jl} r^{-1} z^l [1 + A_1^{jl} z^2 + O(z^4)]$$
$$= A_0^{jl} k^l r^{(l-1)} [1 + A_1^{jl} z^2 + O(z^4)], \tag{A1}$$

and

$$r^{-1} y_l(z) = A_0^{yl} r^{-1} z^{-(l+1)} [1 + A_1^{yl} z^2 + O(z^4)]$$
$$= A_0^{yl} k^{-(l+1)} r^{-(l+2)} [1 + A_1^{yl} z^2 + O(z^4)], \tag{A2}$$

where the coefficients A are real constants, and $|A_1^{jl}|$ and $|A_1^{jl}|$ are <1 regardless of l (Abramowitz & Stegun 1965). Exactly the same expansion form can be obtained for $r^{-1}[j_l(z) + z(dj_l(z)/dz)]$ and $r^{-1}[y_l(z) + z(dy_l(z)/dz)]$ with other sets of real constants. On the other hand, the radial dependence of the analytic solution for Laplace's equation (i.e. $\sigma_{air} = 0$ in eqs 1–3) is $r^{(l-1)}$ and $r^{-(l+2)}$, which represent the external and internal fields, respectively.

Consider further the hypothetical situation where the spatial form of the **H** fields in the earth remains the same, regardless of the choice of governing equation in the air, or the air conductivity. We choose the complex constants for the respective spherical harmonic terms in the air so that the total **H** field values agree with those on the earth's surface. The difference in the decay (for the internal terms) or the growth (for the external terms) versus r in the air layer of the Helmholtz and Laplace equation solutions is of $O(|z^2|)$ when $|z^2| \ll 1$. Considering the period range 2 day $\leq T \leq 1$ yr, and assuming an air conductivity of $\sigma_{air} = 10^{-10}$ S m^{-1}, $|z^2| \leq 1.9 \times 10^{-5}$ when $r < 10 r_e$. For the same value of r, when $\sigma_{air} = 10^{-14}$ S m^{-1}, $|z^2| \leq 1.9 \times 10^{-9}$.

Thus, forward solutions for **H** of Laplace's equation ($\sigma_{air} = 0$) and of the Helmholtz equation with $\sigma_{air} = 10^{-14}$ S m^{-1} and $\sigma_{air} = 10^{-10}$ S m^{-1} should agree within the air layer to within these very small differences. Moreover, if we consider a problem with an external source field with only a P_1^0 term, the magnitude of the internally induced field at the Dirichlet boundary ($r = 10 r_e$) decays to $<10^{-3}$ of the external field intensity. This is true even if we assume the extreme case where the ratio between internal and external field intensities is unity at the air–earth interface. Thus, we can safely solve the forward problem with this Dirichlet boundary value assignment, with the assurance that imposing a small but non-zero air conductivity does not introduce significant inaccuracy.